ROYAL SOCIETY
OF CHEMISTRY

PAPER

Check for updates

Rational design of copper(I)-doped metal–organic frameworks as dual-functional nanocarriers for combined chemo–chemodynamic therapy†

Lijia Yao, [iD] [a] Bingquan Chen,[b] Hailong Wu,[a] Yuanjing Cui [iD] *[a] and Guodong Qian [iD] *[a]

Combination therapies are an increasingly important part of the antitumor medicine armamentarium. However, developing desirable nanomaterials for combination therapies is still a great challenge. Herein, a biocompatible Cu(I)-doped metal–organic framework (MOF) (denoted as CuZn-ZIF) is designed as a novel dual-functional nanocarrier. Doxorubicin molecules are covalently bound to the surface of the CuZn-ZIF and released by the cleavage of chemical bonds in an acidic environment, demonstrating the capacity of controlled drug release. More importantly, CuZn-ZIF nanocarriers can simultaneously play the role of nanocatalysts, capable of catalyzing H_2O_2 into a highly reactive intracellular toxic hydroxyl radical (•OH). An *in vivo* study reveals that nanoparticles exhibit high antitumor efficacy through the combined performance of DOX and Cu(I), proving the great potential of this copper(I)-based MOF for combined chemo-chemotherapy to improve therapeutic efficacy.

1. Introduction

Cancer, one of the most destructive diseases, has posed a serious threat to public health.[1] Chemotherapy,[2] surgery,[3] and radiotherapy,[4] commonly used therapies in clinical cancer treatment, are limited by poor precision, serious side effects, and the frequent emergence of drug resistance.[5] To date, new therapeutic strategies, such as chemodynamic therapy (CDT),[6] phototherapy[7] and immunotherapy,[8] have been widely developed to improve the therapeutic effect, benefiting from their advantages of low side effects, non-invasiveness and facile operation.[9] Despite these advantages, there are still some critical challenges, limiting their potential clinical application. For example, the insufficient concentration of H_2O_2 in tumors restricts the therapeutic efficacy of CDT.[10] Combination therapy is proposed and developed for overcoming the inherent limitations, meanwhile minimizing systemic side effects and accessing the outstanding precision and high therapeutic effects.[11–13] In the past few decades, multifunctional nanomaterials have been designed by integrating two or more therapeutic strategies for combination

therapy.[14] However, they have problems with initial burst and off-target release, resulting in decreased therapeutic efficacy.
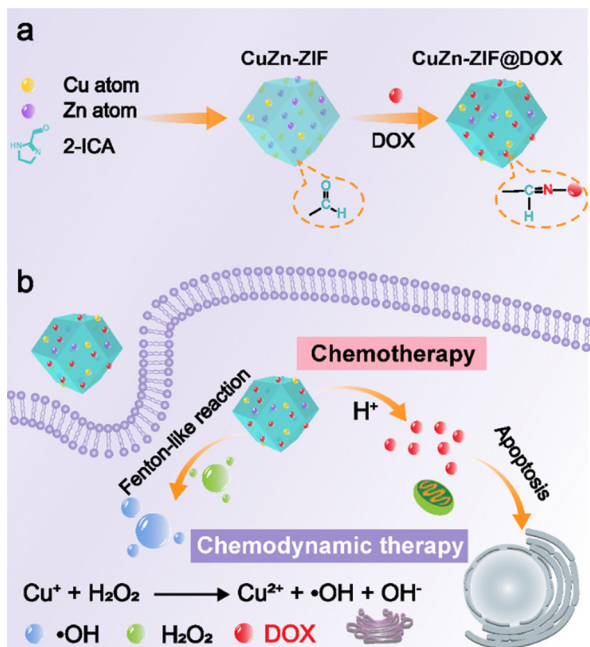
Nanoscale metal–organic frameworks (nMOFs), which are self-assembled by metal ions and organic ligands,[15–19] have great promise in the field of biomedical applications due to their structural diversity, synthetic modularity, permanent porosity and multifunctionality.[20–24] Functional metal ions or organic ligands make it possible to prepare nMOFs with intrinsic antitumor activity for combination therapy.[25–28] High porosity and a large pore/cage structure make nMOFs ideal for drug delivery. Some types of nMOFs can be degraded in the tumor microenvironment (TME), having the potential for targeted drug delivery.[29,30] Zeolitic imidazole framework-90 (ZIF-90), consisting of imidazole-2-carboxaldehyde (2-ICA) and Zn^{2+}, is widely studied in biomedical applications for its biocompatibility, and the properties of ATP/pH-responsive decomposition.[31–34] Especially, the aldehyde group of ZIF-90 provides a facile functional position for post-modification. For example, doxorubicin (DOX) can be covalently bound to ZIF-90.[35] Furthermore, the metal nodes of ZIF-90 can be partially replaced by Fenton ions or Fenton-like ions, including Mn^{2+}, Fe^{2+}, and Cu^{2+} by ion exchange.[36–38] It inspires us to utilize ZIF-90 as a multifunctional nanoplatform based on both the post-modification of organic ligands and ion doping. Considering undesirable doping efficiency and structural destruction during ion exchange, the rational design and synthesis of multifunctional ZIF-90 remain challenging.[39]

In this work, we constructed a dual-functional nanocarrier named CuZn-ZIF *via in situ* crystallization with DOX drugs covalently connected to the surface of the CuZn-ZIF through a

[a] *State Key Laboratory of Silicon and Advanced Semiconductor Materials, ZJU-Hangzhou Global Scientific and Technological Innovation Center, School of Materials Science and Engineering, Zhejiang University, Hangzhou 310027, China. E-mail: cuiyj@zju.edu.cn, gdqian@zju.edu.cn*
[b] *Department of Anaesthesiology, The First Affiliated Hospital, Zhejiang University School of Medicine, Hangzhou, 310003, China*
† Electronic supplementary information (ESI) available. See DOI: https://doi.org/10.1039/d3tb01869e

10632 | *J. Mater. Chem. B*, 2023, **11**, 10632–10639

This journal is © The Royal Society of Chemistry 2023

Scheme 1 (a) The preparation process of CuZn-ZIF@DOX. (b) Schematic illustration of CuZn-ZIF@DOX applied for combining chemotherapy and chemodynamic therapy.

post-synthetic modification method for combining chemotherapy and chemodynamic therapy in tumor treatment (Scheme 1). In general, the multifunctional nanoplatform has the following characteristics, including (1) controllable particle size, which is the prerequisite for CuZn-ZIF@DOX to be used in antitumor therapy, (2) high doping content and a maintained structure, which can prevent the premature release of copper ions, and is conducive to improving the biosafety of copper-based nanocatalytic materials, and (3) pH-independent catalytic properties and pH-responsive drug release, minimizing the off-target effect and serious side effects, and hence effectively induce tumor suppression in tumor-bearing mice.

2. Materials and methods

2.1. Materials

Anhydrous copper acetate (Cu(CH$_3$COO)$_2$, $\geq$98%) was purchased from Aladdin. Zinc acetate (Zn(CH$_3$COO)$_2$, $\geq$99.0%) and imidazole-2-formaldehyde (ICA, $\geq$98%) were purchased from TC. Doxorubicin·HCl was purchased from Meilunbio. The 3-(4,5-dimethylthiazol-2-yl)-2-diphenyltetrazolium bromide (MTT) assay was purchased from KeyGEN BioTECH Corp., Ltd. *N*,*N*-dimethylformamide (DMF, AR) and anhydrous methanol (MeOH, AR) were purchased from Sinopharm. All reagents were commercially available and used without further purification.

2.2. Synthesis of CuZn-ZIF and CuZn-ZIF@DOX

Synthesis of CuZn-ZIF: CuZn-ZIF nanoparticles were synthesized according to the literature with some modifications.[40] First, 10 mM Zn(CH$_3$COO)$_2$ DMF solution (solution A), 10 mM

Cu(CH$_3$COO)$_2$ DMF solution (solution B), and 20 mM ICA DMF solution (solution C) were prepared. Solution D was prepared by mixing solution A with B at different molar ratios (8.5 : 1.5, 9 : 1, 9.5 : 0.5, and 1 : 0). Later, the specific synthesis steps are as follows: 10 mL solution C and 10 mL solution D were injected simultaneously into a round-bottomed flask which contained 10 mL solution C, at different rates under stirring. The products were collected by centrifugation, rinsed by DMF and methanol twice, respectively, and dried in a vacuum oven at 60 °C for 12 hours. About 16 mg powders were obtained. The reaction yield was calculated to be around 63% based on metal salts. Finally, the powder was stored at room temperature for further use.

Synthesis of CuZn-ZIF@DOX: CuZn-ZIF and DOX with different mass ratios were stirred in methanol at room temperature for two days. The products were centrifuged and rinsed three times with methanol. The products were dried in a vacuum oven, and stored in a refrigerator at 4 °C.

2.3. Detection of •OH produced by CuZn-ZIF

The •OH produced by CuZn-ZIF was detected by DMPO through electron spin resonance spectroscopy. In detail, first, 2 mL of sodium acetate buffer solution containing DMPO (25 mM) and H$_2$O$_2$ (100 μM) was prepared. Then, 40 μL of the 1 mg mL^{-1} CuZn-ZIF aqueous dispersion solution was added. After incubating for 5 minutes, the ESR spectra were collected.

2.4. Drug release experiment

The CuZn-ZIF@DOX aqueous dispersion system (5 mg mL^{-1}) was added into dialysis bags (interception MWCO = 3500 Da), and then soaked into phosphate buffered saline at different pH values (pH 7.4, pH 6.5, and pH 5.5). Drug release experiments were performed at 37 °C under stirring. 1 mL solution was collected for further testing to determine the amount of released DOX. Meanwhile, 1 mL of fresh solution was added.

2.5. Cellular experiment

2.5.1. Cell culture. HeLa cells were cultured in the high-glucose DMEM containing 10% fetal bovine serum (FBS) and 1% (penicillin and streptomycin) under a humidified atmosphere with 5% CO$_2$ at 37 °C. HL-7702 (L02, human normal liver cells) cells were cultured in RPMI 1640 containing 10% fetal bovine serum (FBS) and 1% (penicillin and streptomycin) under the same conditions.

2.5.2. Cellular uptake. HeLa cells were incubated in a confocal dish for 4 h. After this, the medium was replaced with a fresh medium containing 100 μg mL^{-1} CuZn-ZIF@DOX. After incubation for 4 h and 8 h, the cells were washed three times with PBS. Then, the cells were fixed with 4% paraformaldehyde for 30 minutes. Finally, the HeLa cells were observed by confocal laser scanning microscopy (CLSM) to observe cell uptake.

2.5.3. Intracellular ROS detection. Intracellular ROS were detected by 2′,7′7tracellular ROS were detec diacetate (DCFH-DA). HeLa cells were inoculated into confocal dishes and incubated for 4 h. After this, the media were replaced with

fresh media containing 100 μg mL^{-1} ZIF-90, CuZn-ZIF, and CuZn-ZIF@DOX, respectively. After incubation for 8 h, the cells were rinsed with PBS and then incubated with DCFH-DA (10 μM) for another 20 minutes. Finally, cells were rinsed with PBS and the fluorescence imaging was conducted on CLSM.

2.5.4. Cytotoxicity of CuZn-ZIF and CuZn-ZIF@DOX. Cell compatibility was assessed using normal cell lines. Briefly, cells were seeded into 96-well plates for 4 h. Then, the medium was removed and replaced with the fresh medium containing different concentrations of CuZn-ZIF (0–150 μg mL^{-1}). After 24 h incubation, 50 μL of 1 × MTT solution was added to each well and incubated for another 4 h. The absorbance was measured using a microplate reader at 492 nm. For the anti-tumor cell ability of CuZn-ZIF and CuZn-ZIF@DOX, HeLa cells were co-cultured with the fresh medium containing different concentrations of CuZn-ZIF and CuZn-ZIF@DOX (Cu, 0–1 μg mL^{-1}; DOX, 0–1.6 μg mL^{-1}) for 24 h or 48 h. The cell viability was measured using the microplate reader at 492 nm.

2.5.5. Live/dead cell staining. Live/Dead cell staining was carried out using calcein-AM/PI staining. Briefly, HeLa cells were seeded in confocal dishes at 1×10^5 cells per dish. After 4 h, HeLa cells were treated with ZIF-90, CuZn-ZIF, and CuZn-ZIF@DOX and incubated for another 24 h, followed by dying with calcein AM and PI and observation at 480 nm.

2.6. *In vivo* antitumor study

All animal experiments were performed based on the relevant laws and institutional guidelines, and the experiments were approved by Ethics Committee of Sir Run Shaw Hospital. Healthy nude mice were purchased from the Laboratory Animal Company of Shanghai Slac. HeLa cells were digested and suspended in the DMEM at a concentration of 1.5×10^7 cells, and 100 μL of aliquots were subcutaneously injected under the arm. Mice were used for further experiments when the tumor size grew to ∼100 mm^3, and the mice were assigned to three groups ($n = 5$ per group) including saline, CuZn-ZIF, and CuZn-ZIF@DOX group. Mice-bearing HeLa cells were intratumorally injected with 100 μL of 4 mg mL^{-1} CuZn-ZIF and CuZn-ZIF@DOX. Tumor volume and body weight were measured every two days. The tumor volume (V) can be calculated according to the following formula: $V = (L \times W^2)/2$, where L and W correspond to the longest and shortest diameters of the tumor, respectively. After 14 days of treatment, all mice were killed, and the major organs (heart, liver, spleen, lung, and kidney) and tumors were sliced and stained with hematoxylin and eosin (H&E). The tumor slices were stained with TUNEL and Ki67. In addition, the obtained tumors were photographed and weighed.

3. Results and discussion

3.1. Synthesis and characterization of CuZn-ZIF

Cu(I) ions or Cu(I)-based nanoparticles are widely studied as effective Fenton-like catalysts, which can catalyze H$_2$O$_2$ to generate •OH and thus result in cell death. However, Cu(II) ions are susceptible to an acidic environment, a main feature of

TME, leading to the reduction of catalytic activity. Some reports revealed that Cu(I) can be stabilized by coordinating Cu(I) with organic molecules. Additionally, the synthesis of nanoscale MOFs with uniform particle sizes and high crystallinity is also a main challenge. Based on classical crystal growth theory, separating the nucleation and growth process is the key to obtaining uniform nanoparticles. In this work, a series of Cu-doped ZIF-90 (CuZn-ZIF) with different sizes and copper content were synthesized by kinetic control according to the literature with some modifications.[40] Typically, based on the classical nucleation theory, burst nucleation is induced by the rapidly increasing concentration over a specific status of supersaturation. Additionally, the nucleation rate is positively correlated to the nuclei density, resulting in smaller nano-particles.

Here, the component was first optimized and the relation-ship between the component and size was revealed. A series of ratios of the anhydrous cupric acetate to zinc acetate were used as the precursor salt solution, and CuZn-ZIF was immediately synthesized by mixing precursor salt solution and imidazole-2-carboxaldehyde solution at different feed rates. Furthermore, the properties of CuZn-ZIF were evaluated by scanning electron microscopy (SEM) and powder X-ray diffraction (PXRD)

Fig. 1 (a) Simulated PXRD patterns of ZIF-90 and experimental PXRD patterns of CuZn-ZIF with different molar ratios of copper to zinc. (b) SEM images of the representative CuZn-ZIF with different molar ratios of copper to zinc and at different feed rates (i) 0.5 : 9.5, 235 mL h^{-1}; (ii) 1.5 : 8.5, 235 mL h^{-1}; (iii) 0.5 : 9.5, 24 mL h^{-1}; (iv) 1.5 : 8.5, 24 mL h^{-1}. Scale bar: 500 nm.

10634 | *J. Mater. Chem. B*, 2023, **11**, 10632–10639

This journal is © The Royal Society of Chemistry 2023

(Fig. 1 and Fig. S1, ESI†). Fig. 1a shows the powder X-ray diffraction patterns of the as-synthesized samples of CuZn-ZIF. The PXRD patterns of CuZn-ZIF match well with the simulated pattern of ZIF-90, indicating that the CuZn-ZIF was synthesized successfully with the same crystal structure as ZIF-90. No obvious impurity diffraction peaks appear after Cu(ɪ) doping, demonstrating the phase purity of the obtained CuZn-ZIF. In addition, the narrow diffraction peaks further imply the high crystallinity of the CuZn-ZIF (Fig. 1a). Fig. 1b shows the SEM images of CuZn-ZIF selected from Fig. S1 (ESI†), apparently showing the relationship among the particle sizes, feed rates, and Cu/Zn molar ratios. As shown in Fig. 1b and Fig. S2 (ESI†), the morphology of the CuZn-ZIF is the rhombic dodecahedron and the particle size of CuZn-ZIF is negatively correlated with the feed rates and positively correlated with the copper content. Remaining of the content of copper at 15% (the molar ratio of copper to zinc is $1.5 : 8.5$), smaller particles of CuZn-ZIF were synthesized at a faster feed rate, and the nanoparticles synthesized at 235 mL h^{-1} feed rate are the smallest, which is consistent with the previous result.[40] It is because a higher feed rate in the early stage will accelerate the nucleation rate of the material, resulting in a large number of crystal nuclei. Since the total amount of raw material is certain, the increase of the crystal nucleus will reduce the average particle sizes of the final product. Similarly, the increase of the Cu/Zn ratio in the raw material is equivalent to reducing the feed rate of Zn^{2+}, thereby reducing the nucleation rate, and ultimately leading to an increase in the average size of particles. The maximum copper content in CuZn-ZIF was explored. Under 235 mL h^{-1} of the feed rate, when the ratio of Cu/Zn was continuously increasing to 2/8, the synthesized products were too large, accompanied by the appearance of quadratic nucleation (Fig. S3, ESI†).

Note that the reduction in the size of the particles is vital for further biological applications and the large number of Cu active sites would lead to better Fenton-like catalytic efficacy. Therefore, 15% of the Cu content in the precursors (the molar ratio of Cu^{2+}/Zn^{2+} is $1.5 : 8.5$) and 235 mL h^{-1} feed rate were selected to prepare the CuZn-ZIF with 137 nm in diameter, based on the TEM image (Fig. 2a), the SEM image (Fig. S1, ESI†) and dynamic light scattering (DLS) in water (Fig. 2c). The high angle annular dark field scanning TEM (HAADF-STEM) images and energy dispersive X-ray spectroscopy (EDS) mapping suggest that Cu, Zn, C, N, and O are homogenously distributed on the particle, verifying the high-purity and high-quality of as-prepared NPs (Fig. 2b). The actual content of copper in CuZn-ZIF determined by inductively coupled plasma (ICP) is 2.6 wt% (Table S1, ESI†). N$_2$ adsorption–desorption isotherm

Fig. 2 Characterization of CuZn-ZIF. (a) The representative TEM image, (b) the elemental mapping image, and (c) the size distribution of CuZn-ZIF (added Cu^{2+}/Zn^{2+} = 1.5/8.5). To identify the valence state of copper in CuZn-ZIF, (d) a high-resolution XPS spectrum of Cu 2p for the CuZn-ZIF and (e) FT-IR spectra of ZIF-90 and CuZn-ZIF were analyzed. (f) ESR spectra of CuZn-ZIF at different pH values in the presence of DMPO were monitored to study the capacity of •OH generation. (g) CLSM images of HeLa cells under different treatments to evaluate ROS production with DCFH-DA as a fluorescent probe. Scale bar: 80 μm.

This journal is © The Royal Society of Chemistry 2023

J. Mater. Chem. B, 2023, **11**, 10632–10639 | **10635**

curves reveal that ZIF-90 and CuZn-ZIF featured Brunauer–Emmett–Teller (BET) specific surface areas of 1323 m^2 g^{-1} and 1044 m^2 g^{-1}, respectively (Fig. S4, ESI†). It should be noted that pristine ZIF-90 exhibited a type-IV isotherm, in which a small step at 0.35 relative pressure accompanied by a hysteresis loop (ranging from 0.35–0.58 relative pressure) is observed, indicating that the ZIF-90 samples contain mesopores, which could induce capillary condensation, due to cracks or defects generated in crystal formation.[41] The hysteresis disappears and the isotherm changes gradually to type-I upon when introducing copper ions. The thermal stability of CuZn-ZIF is shown in Fig. S5 and S6 (ESI†), and the first stage with weight loss of 5.5% between 40 and 100 °C resulted from the removal of physically absorbed water. The second stage from 180 °C to 400 °C displayed the degradation of CuZn-ZIF, attributing to the decomposition of the ZIF linkers.[42] The onset degradation temperature of CuZn-ZIF (226 °C) is slightly lower than that of ZIF-90 (289 °C), indicating weakened thermal stability after Cu(I) doping. The DSC curves demonstrated the sharp exothermic DSC peak at around 312 °C and 246 °C of ZIF-90 and CuZn-ZIF, consistent with the decomposition of residual linker supporting TGA results.[43,44]

It is well-known that the valence state of Cu plays a key role in Fenton-like activity. Thus, the valence state of Cu in CuZn-ZIF was evaluated, and X-ray photoelectron spectroscopy (XPS) was used to give further insight (Fig. 2d and Fig. S7, ESI†). It clearly shows two main peaks at ~932.1 eV and 951.85 eV with a spin energy separation of 19.75 eV are attributed to Cu $2p_{3/2}$ and Cu $2p_{1/2}$ of CuZn-ZIF respectively, suggesting that the Cu atoms in CuZn-ZIF are mainly in the +1 oxidation state.[45] Besides, no satellite peak related to Cu(ii) appears. We presumed that the –CHO of imidazole-2-formaldehyde acts as a reductant under synthetic conditions and generates Cu(ii)

during the reaction.[46] FT-IR tests were performed to explain the cause of the change of copper valence (Cu(ii) → Cu(i)) during the synthesis of CuZn-ZIF (Fig. 2e). The peak at 1675 cm^{-1} in the ZIF-90 spectrum is assigned to the C=O stretching frequency of -CHO. Upon the introduction of Cu(ii) ions, the intensity of the peak significantly decreased and a shoulder band at 1612 cm^{-1} appeared. According to the reported literature,[47] this shoulder peak could be explained by intramolecular hydrogen bonding of the carbonyl groups in the enol form, confirming the presence of a carboxyl group in the CuZn-ZIF.

Furthermore, the valence variation of the Cu element after incubation with H_2O_2 aqueous solution (30 wt%) was also evaluated (Fig. S7b and d, ESI†). After reacting with H_2O_2, the Cu(i)/Cu(ii) ratio of CuZn-ZIF varied from 100% to 83.5%, indicating partial Cu(i) partially oxidized to Cu(ii). In terms of its reactivity towards H_2O_2, CuZn-ZIF has the potential for nanocatalytical medicine that can drive cell death by generating $^{\bullet}OH$ through the copper-based Fenton-like reaction analogous to the Fe^{2+}/H_2O_2 system (Equation: $Cu^+ + H_2O_2 \rightarrow Cu^{2+} + OH^- + {^{\bullet}OH}$). Then, electron spin-resonance (ESR) measurement was carried out to identify the generation of $^{\bullet}OH$ by using 5, 5-dimethyl-pyrroline-N-oxide (DMPO) as the $^{\bullet}OH$ trapping agent (Fig. 2f). The ESR spectra of CuZn-ZIF show a 1:2:2:1 quartet characteristic of DMPO-OH after the addition of DMPO, demonstrating that CuZn-ZIF could catalyze H_2O_2 into $^{\bullet}OH$. Besides, CuZn-ZIF has great catalytic activity in both acidic (pH 5.0) and neutral (pH 7.4) environments, showing pH-independent catalytic properties. To verify the capacity of producing $^{\bullet}OH$ at the cellular level, 2′,7′7erify the capacity of produdiacetate (DCFH-DA) was used as a reactive oxygen probe to detect the intracellular cellular ntHeLa cells. The brighter fluorescence displayed in the CuZn-ZIF group illustrates that

Fig. 3 (a) TEM image of CuZn-ZIF@DOX. (b) Size distribution of CuZn-ZIF@DOX. (c) PXRD patterns of CuZn-ZIF@DOX. (d) UV-vis spectra of ZIF-90, CuZn-ZIF, CuZn-ZIF@DOX, and DOX (inset: the enlarged figure). (e) The loading efficiency and loading capacity of DOX to CuZn-ZIF at a series of mass ratios. (f) The release of DOX from CuZn-ZIF@DOX at different pH values.

10636 | *J. Mater. Chem. B*, 2023, **11**, 10632–10639

This journal is © The Royal Society of Chemistry 2023

CuZn-ZIF could promote the production of $\cdot OH$ in tumor cells (Fig. 2g). All above, the controllable size of nanoparticles, and the existing Cu(I) make CuZn-ZIF ready for intracellular drug delivery and chemodynamic therapy.

3.2. DOX loading and release properties

DOX as a chemotherapy drug has been shown to regulate the concentration of intracellular GSH and H_2O_2 by inducing mitochondrial apoptosis, which can be used to enhance the effect of CDT. However, free DOX has the disadvantages of burst release and serious toxicity in normal tissues.[48] Using nanomaterials can promote the enrichment of DOX at the tumor sites and improve the efficiency of tumor treatment. Based on the above considerations, DOX-loaded CuZn-ZIF (CuZn-ZIF@DOX) was prepared using the Schiff base reaction. The particle size of CuZn-ZIF@DOX is about 158 nm according to the TEM image (Fig. 3a) and DLS measurement (Fig. 3b). And the crystal structure is maintained after the reaction (Fig. 3c). Here, UV-vis absorption spectroscopy was used to characterize the loading of DOX. As shown in Fig. 4d, a new absorption band among 520–620 nm appears in the absorption spectrum of CuZn-ZIF@DOX, corresponding to the adsorption of DOX. It is worth noting that the absorption peak of DOX of the composite has a significant redshift compared to the original DOX (480 nm), which could be ascribed to the deprotonation of

the amino group during the reaction.[49] The FT-IR spectrum results show a new absorption peak at 1072 cm^{-1} belonging to DOX, also indicating the successful loading of DOX (Fig. S8, ESI†).

Noteworthily, the new peak located at 1574 cm^{-1} can be considered as C=N bonds, proving the covalent interaction between the amino group of DOX and the aldehyde group of 2-formylimidazole. XPS results also reveal the interaction between DOX and CuZn-ZIF (Fig. S9, ESI†). The C 1s spectrum of CuZn-ZIF@DOX presents a new shoulder peak at 286 eV that is derived from DOX and a slight shift of the peak might result from the interaction with CuZn-ZIF.

By varying the mass ratio of MOFs to DOX, the loading capacity and loading efficiency of DOX were measured (Fig. 3e and Fig. S10, ESI†). According to the loading curve, the maximum loading capacity is 9 wt%. The crystal structure of CuZn-ZIF was maintained after being loaded with different contents of DOX (Fig. S11, ESI†). Upon surface covalent attachment, DOX molecules lead to a slight specific surface area change of CuZn-ZIF (1029 cm^2 g^{-1} against 1044 cm^2 g^{-1} for loaded and unloaded nanoparticles, respectively) (Fig. S4, ESI†). Meanwhile, it has a negligible impact on the catalytic activity of CuZn-ZIF (Fig. S12, ESI†). According to the XPS results of CuZn-ZIF@DOX, the peak at 932.8 eV of CuZn-ZIF@DOX corresponds to Cu(I) 2p$_{3/2}$ (Fig. S13, ESI†).
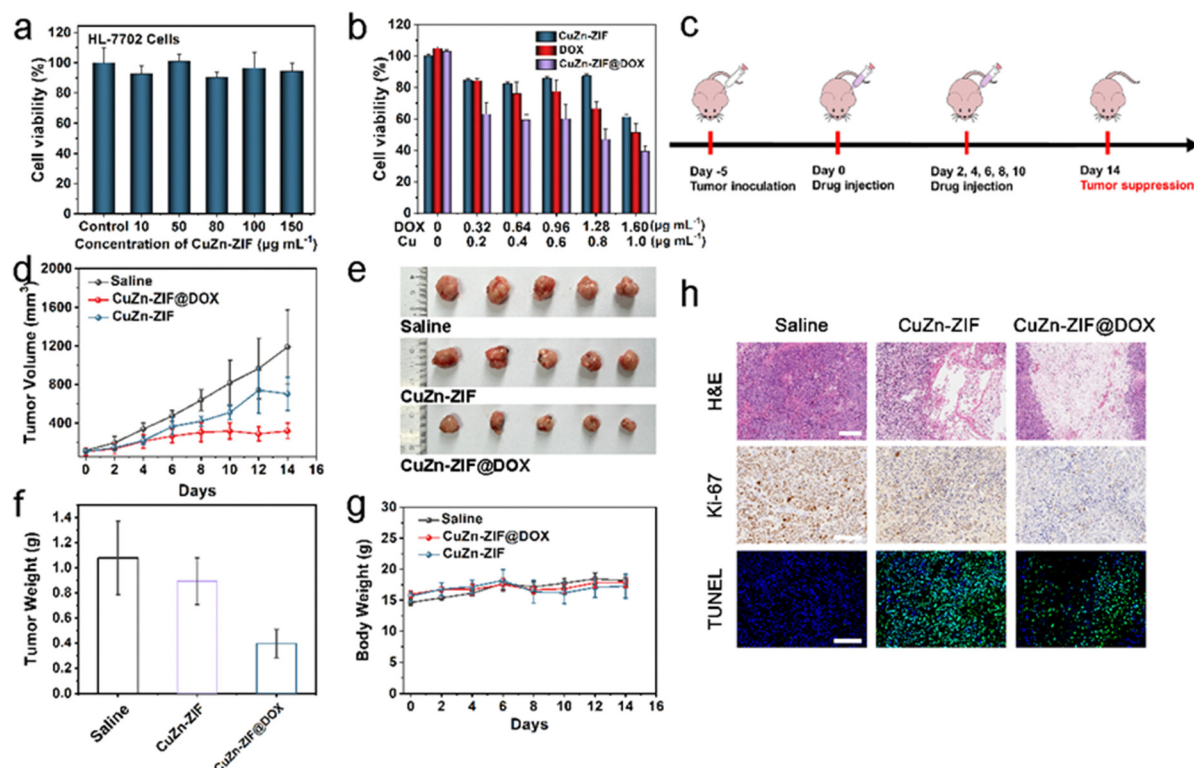

Fig. 4 (a) Cell viability of HL-7702 after incubation with CuZn-ZIF at different concentrations. (b) Cell viability of HeLa cells after incubation with CuZn-ZIF, DOX, and CuZn-ZIF@DOX for 24 h. (c) HeLa tumor–bearing mice were treated by intratumoral (i.t.) administration on days 0, 2, 4, 6, 8, and 10, and the tumor growth (d) was monitored. (e and f) Photographs of tumors and the graph of tumor weight after 14 days treatment. (g) Body weight variation of mice under different treatments during 14 days. (h) H&E, Ki-67, and TUNEL stained images of tumors after different treatments. Scale bar: 100 μm.

This journal is © The Royal Society of Chemistry 2023

J. Mater. Chem. B, 2023, **11**, 10632–10639 | **10637**

To evaluate the drug release behavior of CuZn-ZIF@DOX, the drug release experiment was carried out as follows. CuZn-ZIF@DOX particles were dispersed in a phosphate buffer solution at pH 7.4, 6.5, and 5.5. As shown in Fig. 3f, only 2.2% DOX was released from CuZn-ZIF@DOX at pH 7.4, while the release rate of DOX increased in a slightly acidic solution. During 10 hours, the released amounts of DOX were up to 43.3% and 76.1% in the acidic solution at pH 6.5 and pH 5.5, respectively. Such talented capacity of pH-responsive drug release is attributed to the pH-sensitive covalent bond (C=N) between DOX and CuZn-ZIF, which is prone to breaking in an acidic environment.

3.3. Cellular uptake and *in vitro* cytotoxicity

For cellular experiments, an *in vitro* cellular uptake experiment was conducted in the HeLa cell line. Specifically, CuZn-ZIF@DOX was co-incubated with HeLa cells for 4 h and 8 h, and a confocal laser scanning microscope (CLSM) was used for observation (Fig. S14, ESI†). After four hours of incubation, red fluorescence emitted by DOX is detected in HeLa cells. The intensity of red fluorescence strengthens when the incubation time increases to 8 h, illustrating the continuous release of DOX from CuZn-ZIF@DOX. Notably, a few HeLa cells die in the presence of the irregular shape of the nucleus and the reduced cytoplasmic volume, as a result of the apoptosis effect of DOX.

Later, the cytotoxicity of CuZn-ZIF is assessed using the 3-(4, 5-dimethylthiazol-2-yl)-2,5-diphenyltetrazolium bromide (MTT) assay in HL-7702 cells (human hepatocytes cells) and HeLa cells (cervical cancer cells). CuZn-ZIF with a series of concentrations is co-incubated with HL-7702 cells for 24 h. According to MTT results (Fig. 4a), the cell viability sustains over 80% when the concentration of CuZn-ZIF is high to 150 $\mu g\ mL^{-1}$, indicating that CuZn-ZIF is nearly non-toxic to normal cells, whereas the nanoparticles prefer to inhibit the proliferation of HeLa cells (Fig. 4b). When treated with 200 μL CuZn-ZIF containing 0.2 μg Cu atoms (1 $\mu g\ mL^{-1}$ of Cu atoms), partial HeLa cells die and the cell viability decreases to 40%, attributing to the production of highly toxic $^{\bullet}OH$ by CuZn-ZIF through the Fenton-like reaction with overexpressed H_2O_2 in tumor cells. The additionally introduced H_2O_2 could enhance the reaction (Fig. S15, ESI†), and further result in a higher cell inhibition effect. Additionally, the group treated with CuZn-ZIF@DOX shows the highest inhibition effect, whereas CuZn-ZIF@DOX with 0.64 $\mu g\ mL^{-1}$ DOX causes 60% cell death. When prolonging the incubation time to 48 h, the cell viability decreases to 20% (Fig. S16, ESI†). Moreover, HeLa cells after the treatment of PBS, ZIF-90, CuZn-ZIF, and CuZn-ZIF@DOX were co-stained with calcein-AM/propidium iodide for presenting the viability more directly where red fluorescence and green fluorescence represent dead and live cells, respectively (Fig. S17, ESI†). The results are consistent with the above MTT results that the HeLa cells treated CuZn-ZIF@DOX are nearly completely dead.

3.4. *In vivo* therapeutic efficacy on HeLa tumor-bearing nude mice

The excellent tumor cell-killing effect *in vitro* of CuZn-ZIF and CuZn-ZIF@DOX encourages us to further study their antitumor effect *in vivo*. CuZn-ZIF@DOX is administered by intratumor (i.t.) injection in HeLa tumor-bearing mice to assess its anti-tumor activity. The establishment of a tumor-bearing nude mice model and the treatment process is briefly illustrated in Fig. 4c. The tumor-bearing nude mice are divided into three groups under different treatments, including saline (1) CuZn-ZIF (2), and CuZn-ZIF@DOX (3). These mice are treated intra-tumorally with the particles at a dose of 20 mg kg^{-1}. During a two-week treatment, the body weight and tumor volume are recorded every other day. As shown in Fig. 4d–f, the tumor growth is restricted in the CuZn-ZIF group and CuZn-ZIF@DOX group. The tumor inhibition rate reaches 17.3% in the CuZn-ZIF group owing to the effect of CDT. Additionally, the higher tumor inhibition effect could be observed in the CuZn-ZIF@DOX group, where the inhibition rate reaches 63.4%. The impressive therapeutic effect is achieved by the synergistic effect of chemotherapy and chemodynamic therapy originating from DOX and Cu(I). Next, hematoxylin and eosin (H&E) staining of tumor slices from different groups is performed to evaluate the therapeutic efficiency (Fig. 4h). As noticed, mice treated with CuZn-ZIF or CuZn-ZIF@DOX suffer a high level of tumor cell apoptosis and necrosis, validating the Cu(I)-mediated chemodynamic effect. Moreover, CuZn-ZIF@DOX triggers the most prominent tumor tissue damage, resulting from the combined effect of CDT and chemotherapy. Furthermore, Ki-67 and TUNEL staining are conducted on tumor slices to study the tumor cell proliferation and apoptosis levels. The least brown area CuZn-ZIF@DOX group indicates its excellent inhibiting effect on the proliferation of tumor cells. Meanwhile, the highest level of TUNEL staining signals is detected from the CuZn-ZIF@DOX group, implying massive apoptosis of tumor cells.

The body weight of mice treated with nanoparticles increases in the same trend as the control group, verifying the good biocompatibility of the material (Fig. 4g). The bio-compatibility is also assessed by H&E-staining of major organ slices including heart, kidneys, liver, lungs, and spleen (Fig. S19, ESI†). The results show that no significant cytolysis and disruption occurred. Therefore, CuZn-ZIF@DOX has the potential to combine chemotherapy and chemodynamic therapy to realize effective anti-tumor therapy.

4. Conclusions

In this work, we build a new dual-functional nanoparticle (CuZn-ZIF@DOX) as a therapeutic platform for antitumor therapy combining chemotherapy and chemodynamic therapy. CuZn-ZIF nanoparticles with an optimum size (137 nm) and copper content (2.6 wt%) are synthesized by separating the process of nucleation and growth by controlling the feed rates of the original solution. CuZn-ZIF NPs are biocompatible and can act as both nanocatalytic medicine and a drug carrier with a DOX-loaded capacity of 9 wt%. *In vitro* and *in vivo* experiments show that CuZn-ZIF@DOX exhibits combined antitumor

efficacy by producing •OH and releasing DOX, which can effectively inhibit tumor growth.

Conflicts of interest

There are no conflicts to declare.

Acknowledgements

References

1 T. Souho, L. Lamboni, L. Xiao and G. Yang, *Biotechnol. Adv.*, 2018, **36**, 1928–1945.

2 F. Zhang, H. Dong, X. Zhang, X. Sun, M. Liu and D. Yang, *ACS Appl. Mater. Interfaces*, 2017, **9**, 27332–27337.

3 J. Chen, J. Liu, Y. Hu, Z. Tian and Y. Zhu, *Sci. Technol. Adv. Mater.*, 2019, **20**, 1043–1054.

4 C. Allen, S. Her and D. A. Jaffray, *Adv. Drug Delivery Rev.*, 2017, **9**, 27332–27337.

5 L. Sun, Y. Xu, Y. Gao and X. Ning, *Small*, 2019, **15**, 1901156.

6 S. Li, P. Jiang, F. Jiang and Y. Liu, *Adv. Funct. Mater.*, 2021, **31**, 2100243.

7 X. Deng, Z. Shao and Y. Zhao, *Adv. Sci.*, 2021, **8**, 2002504.

8 Q. Li, Y. Liu, Y. Zhang and W. Jiang, *J. Controlled Release*, 2022, **347**, 183–198.

9 J. Yang, D. Dai, X. Zhang and Y. Yang, *Theranostics*, 2023, **13**, 295–323.

10 S. Gao, X. Lu, P. Zhu, H. Lin and J. Shi, *J. Mater. Chem. B*, 2019, **7**, 3599–3609.

11 X. Wang, X. Zhong, Z. Liu and L. Cheng, *Nano Today*, 2020, **35**, 100946.

12 H. Xiang, C. You, W. Liu, D. Wang, Y. Chen and C. Dong, *Biomaterials*, 2021, **277**, 121071.

13 Y. Ma, Z. Su, L. Zhou, L. He, Z. Hou and J. Zou, *Adv. Mater.*, 2022, **34**, 2107560.

14 Z. Zhang, W. Sang, L. Xie and Y. Dai, *Coord. Chem. Rev.*, 2019, **399**, 213022.

15 J. Yang and Y. Yang, *Small*, 2020, **16**, 1906846.

16 D. Zhao, W. Zhang, Z. Wu and H. Xu, *Front. Chem.*, 2021, **9**, 834171.

17 C. Hu, J. Chen, H. Zhang, L. Wu, P. Yang and X. Hou, *Coord. Chem. Rev.*, 2022, **180**, 107595.

18 Z. Zhang, W. Sang, L. Xie and Y. Dai, *Microchem. J.*, 2019, **399**, 213022.

19 P. Horcajada, R. Gref, T. Baati, P. K. Allan, G. Maurin and P. Couvreur, *Chem. Rev.*, 2012, **112**, 1232–1268.

20 M. Bazargan, F. Ghaemi, A. Amiri and M. Mirzaei, *Coord. Chem. Rev.*, 2021, **445**, 214107.

21 M. Nazari, A. Saljooghi, M. Ramezani, M. Alibolandi and M. Mirzaei, *J. Mater. Chem. B*, 2022, **10**, 8824.

22 Z. Rahmati, R. Khajavian and M. Mirzaei, *Inorg. Chem. Front.*, 2021, **8**, 3581.

23 M. Bazargan, M. Mirzaei, A. Franconetti and A. Frontera, *Dalton Trans.*, 2019, **48**, 5476.

24 M. Mirzaei, Z. Karrabi, A. Bauzá and A. Frontera, *CrystEngComm*, 2014, **16**, 5352.

25 W. Cheng, J. Nie, N. Gao, G. Liu, W. Tao and X. Xiao, *Adv. Funct. Mater.*, 2017, **27**, 1704135.

26 G. Chen, Y. Yang, Q. Xu, M. Ling, H. Lin and W. Ma, *Nano Lett.*, 2020, **20**, 8141–8150.

27 J. Xu, Q. Zheng, X. Cheng, S. Hu, C. Zhang and X. Zhou, *J. Nanobiotechnol.*, 2021, **19**, 1–20.

28 T. Wen, G. Quan, B. Niu, Y. Zhou, Y. Zhao and C. Lu, *Small*, 2021, **17**, 2005064.

29 H. Zheng, Y. Zhang, L. Liu, W. Wan, P. Guo and A. Nyström, *J. Am. Chem. Soc.*, 2016, **138**, 962–968.

30 C. He, K. Lu, D. Liu and W. Lin, *J. Am. Chem. Soc.*, 2014, **136**, 5181–5184.

31 X. Yang, Q. Tang, Y. Jiang and L. Mao, *J. Am. Chem. Soc.*, 2019, **141**, 3782–3786.

32 Y. Wang, J. Morrissey, P. Gupta and S. Singamaneni, *ACS Appl. Mater. Interfaces*, 2023, **15**, 18598–18607.

33 Q. Li, H. Luo, Y. Luo and C. Xu, *Chem. Eng. J.*, 2022, **437**, 135369.

34 L. Lu, G. Liu, C. Lin, K. Li and K. Cai, *Adv. Healthcare Mater.*, 2021, **10**, 2100978.

35 Z. Jiang, Y. Wang, L. Sun, B. Yuan and A. Wu, *Biomaterials*, 2019, **197**, 41–50.

36 J. Shen, H. Yu, Y. Shu, M. Ma and H. Chen, *Adv. Funct. Mater.*, 2021, **31**, 2106106.

37 X. Zhao, Y. Wang, W. Jiang, Q. Wang, J. Shi and J. Liu, *Adv. Mater.*, 2022, **34**, 2204585.

38 Y. Wang, D. Zhang, Y. Zeng and P. Qi, *ACS Appl. Mater. Interfaces*, 2023, **15**, 8424–8435.

39 Q. Li, J. Yu, L. Lin, Y. Zhu and L. Tian, *ACS Appl. Mater. Interfaces*, 2023, **15**, 16482–16491.

40 X. Wang, Q. Cheng, Y. Yu and X. Zhang, *Angew. Chem., Int. Ed.*, 2018, **57**, 7836–7840.

41 H. Zhang, M. Li, X. Wang, D. Luo, Y. Zhao and X. Zhou, *J. Mater. Chem. A*, 2018, **6**, 4260–4265.

42 N. Nordin, A. Ismail, A. Mustafa and T. Matsuura, *RSC Adv.*, 2014, **4**, 33292–33300.

43 A. Kumar, V. Mutreja, V. Anand and R. Kataria, *J. Mol. Struct.*, 2023, **1284**, 135365.

44 X. Yang, Q. Yu, W. Gao and X. Tang, *Ceram. Int.*, 2022, **48**, 34148–34168.

45 Z. Guo, C. Li, M. Gao, X. Han and W. Li, *Angew. Chem., Int. Ed.*, 2021, **60**, 274–280.

46 D. Sengupta, P. Melix, S. Bose, J. Duncan and O. Farha, *J. Am. Chem. Soc.*, 2023, **145**, 20492–20502.

47 C. Yen, S. Liu, W. Lo and F. Shieh, *Chem. – Eur. J.*, 2016, **22**, 2925–2929.

48 I. Imosemi, S. Owumi and U. Arunsi, *J. Biochem. Mol. Toxicol.*, 2022, **36**, 1–13.

49 M. Fiallo, H. Tayeb, A. Suarato and A. Garnier-Suillerot, *J. Pharm. Sci.*, 1998, **87**, 967–975.

This journal is © The Royal Society of Chemistry 2023

J. Mater. Chem. B, 2023, **11**, 10632–10639 | **10639**